

High-Resolution Simulations of LS 5039

R. Kissmann¹, D. Huber¹, and P. Gschwandtner²

¹ Institut für Astro- und Teilchenphysik, Leopold-Franzens-Universität Innsbruck, 6020 Innsbruck, Austria
e-mail: ralf.kissmann@uibk.ac.at

² Institut für Informatik, Leopold-Franzens-Universität Innsbruck, 6020 Innsbruck, Austria

Received –; accepted –

ABSTRACT

Context. We present an analysis of our high-resolution relativistic-hydrodynamics model of the stellar- and pulsar-wind interaction in the LS-5039 system.

Aims. With our high-resolution simulation covering three orbital periods, we analyse the impact of turbulence with a particular focus on short-term and orbit-to-orbit variations.

Methods. Our model uses a relativistic hydrodynamics description of the wind interaction in the LS-5039 system assuming a pulsar-wind driven scenario. The corresponding system of equations is solved using the finite-volume code CRONOS. We compute statistical quantities, also relevant for particle acceleration in this system, from results of multiple consecutive timesteps.

Results. In our simulation we find the previously observed shock structures related to the wind-collision region (WCR), including the pulsar-wind termination, being dynamically influenced by orbital motion. In our high-resolution simulation we find high turbulence levels following from instabilities driven at the WCR. These instabilities lead to strong fluctuations of several dynamical quantities especially around and after apastron. These fluctuations are expected to impact the particle transport and also especially the related emission of non-thermal radiation. As an important example, the region from which gamma-ray emission has been found to be boosted due to relativistic beaming in previous studies shows strong variations in size both on short and on orbital timescales.

Conclusions. Using a large computational domain together with high spatial resolution allowed a detailed study of fluctuations in the stellar- and pulsar-wind interaction. The results indicate a possible influence on the non-thermal emission from this system, which will be analysed with dedicated simulations in a forthcoming publication.

Key words. stars: individual: LS 5039 – stars: winds, outflows – hydrodynamics – relativistic processes – gamma rays: stars – methods: numerical

1. Introduction

Gamma-ray binaries are binary systems which consist of a massive star and a compact object and emit the major part of their observable radiative output in the gamma-ray regime. A prominent approach to explain the observed non-thermal emission from some of these systems is the wind-driven scenario (see Dubus 2013, and references therein). In this case, the compact object is assumed to be a pulsar, where the highly relativistic pulsar wind forms a wind-collision region (WCR) when interacting with the massive stellar wind from the star. At the strong shocks surrounding the WCR, particles are thought to be injected and accelerated to very high energies (Maraschi & Treves 1981; Dubus 2006).

The most studied gamma-ray binary is the LS-5039 system, for which a plethora of observations is available at different energies. Additionally, the properties of this system are comparatively well known: it contains an O-type star and a compact object in a mildly eccentric orbit around each other. For this system, many studies assume the wind-driven scenario, where a small fraction of the rotational energy of the pulsar drives a pulsar wind interacting with the wind of the O-type star. This scenario is supported by the orbital modulation observed in the non-thermal emission at different energies (see, e.g. Aharonian et al. 2005; Abdo et al. 2009; Takahashi et al. 2009). Additionally, there is tentative evidence of pulsations in X-rays from an analysis of Suzaku and Nustar data (Yoneda et al. 2020), which also hint at the presence of a pulsar as the compact object. While

Volkov et al. (2021) discuss that the significance of the periodicity found by Yoneda et al. (2020) is rather low, they nonetheless argue from their observation of the lightcurve of LS 5039 that the colliding-wind scenario still is the most likely one.

In this scenario, the non-thermal emission from LS 5039 is strongly linked to the complex dynamics of the colliding pulsar and stellar winds within the WCR and beyond. Correspondingly, this dynamical interaction has already been investigated in many numerical studies. Due to the high numerical cost of a fully relativistic description, early works focussed on individual aspects of such gamma-ray binary systems, where certain simplifications became feasible, like neglect of a relativistic description (Romero et al. 2007; Takata et al. 2012), neglect of orbital motion (Bogovalov et al. 2012; Lamberts et al. 2013; Dubus et al. 2015), or simulations with reduced dimensionality (Bosch-Ramon et al. 2012; Bogovalov et al. 2012; Paredes-Fortuny et al. 2015).

First 3D, relativistic simulations of LS 5039 were discussed in Bosch-Ramon et al. (2015), where in particular the difference to 2D simulations and the evolution of instabilities were studied (see also Bosch-Ramon et al. 2017; Barkov & Bosch-Ramon 2016, for relativistic 3D simulation of other gamma-ray binaries). By using a radially increasing cell size, the authors were able to simulate a larger computational domain, while still having high resolution near the apex of the WCR. Like the previous two-dimensional study Bosch-Ramon et al. (2012), Bosch-Ramon et al. (2015) observed the spiral pattern caused by the

orbital motion, which starts being disrupted at larger radii due to the turbulence driven in the WCR, as also observed in colliding-wind-binary simulations (Lamberts et al. 2012). However, due to the radially decreasing resolution, turbulence was attenuated in the outer parts of the simulations by Bosch-Ramon et al. (2015). While Huber et al. (2021b) used homogeneous resolution through their simulated domain, the authors found that the corresponding domain was too small to contain the unshocked pulsar wind at all orbital phases.

In this work, we extend the previous studies, by investigating a simulation of LS 5039 with homogeneous high spatial resolution throughout the entire numerical domain. In particular we increase the size of the numerical domain as compared to Huber et al. (2021b) and further increase the spatial resolution to reduce the dissipation of turbulence in the simulation. Additionally, we simulate the dynamics of the system for three full orbits, where the first orbit is only used to allow the system to settle into a quasi steady state. With this, we are able to observe the impact of turbulence also in the outer parts of the numerical domain and not only quantify the short-term variation but also the orbit-to-orbit variability of LS 5039.

The paper is structured as follows: in Sec. 2 we introduce the specific setup of our simulation together with the mathematical description. The results are discussed in Sec. 3, where we start by investigating the flow structure and the dynamics and end with an analysis of the short-term and orbit-to-orbit variations. Finally, we summarise our findings in Sec. 4.

2. Physical and Numerical Setup

Since we simulate the interaction of a highly-relativistic pulsar wind with the massive wind of an early-type star, we use relativistic hydrodynamics (RHD) to describe the wind dynamics (for a more extensive discussion of the model see Huber et al. 2021a). In particular, we solve the following set of partial differential equations:

$$\frac{\partial D}{\partial t} + \nabla \cdot \left(\frac{1}{\gamma} D \mathbf{u} \right) = 0 \quad (1)$$

$$\frac{\partial \tau}{\partial t} + \nabla \cdot \left(\frac{1}{\gamma} (\tau + p) \mathbf{u} \right) = S_\tau \quad (2)$$

$$\frac{\partial \mathbf{m}}{\partial t} + \nabla \cdot \left(\frac{1}{\gamma} \mathbf{m} \mathbf{u} \right) + \nabla p = S_m \quad (3)$$

where we have the vector \mathbf{U} of conserved quantities

$$\mathbf{U} = \begin{pmatrix} D \\ E \\ \mathbf{m} \end{pmatrix} = \begin{pmatrix} \gamma \rho \\ \gamma \rho (\gamma h - 1) \\ D \mathbf{h} \mathbf{u} \end{pmatrix}. \quad (4)$$

Here, ρ is the mass density, \mathbf{u} is the spatial vector of the relativistic four velocity with $u^i = \gamma v^i$, h is the specific enthalpy, and p is the thermal pressure. Additionally, τ is related to E via $E = \tau + D$. With our normalisation $c = 1$, \mathbf{v} is given in units of the speed of light and we find for the relativistic Lorentz factor:

$$\gamma = \frac{1}{\sqrt{1 - \mathbf{v}^2}} = \sqrt{1 + \mathbf{u}^2} \quad (5)$$

i.e., the Lorentz factor can be directly computed from the spatial components of the relativistic four velocity.

The system of equations given in Eqs. 1 - 2 is closed by an ideal equation of state:

$$h(\rho, p) = 1 + \frac{\Gamma}{\Gamma - 1} \frac{p}{\rho}, \quad (6)$$

where we use a constant adiabatic exponents $\Gamma = 4/3$ (see Huber et al. 2021a, for a related discussion). Here, we did not solve an equation for E as is often done in other simulations (see, e.g., Mignone et al. 2007), since D and E can become very similar in the low-pressure, non-relativistic regime. With both D and E being conserved quantities, τ is also a conserved, which is more suitable in our case especially for the treatment of the stellar wind. Additionally, we solved a supplementary conservation equation for the specific entropy $s = p/\rho^\Gamma$, which is only conserved in smooth flows, and can there be used to overcome possible problems with negative pressure (see Huber et al. 2021a).

These equations were solved using the CRONOS code (Kissmann et al. 2018), which was recently extended to allow simulations of relativistic hydrodynamics (see Huber & Kissmann 2021). In this work, we applied piecewise linear spatial reconstruction using the minmod limiter (van Leer 1979; Harten et al. 1983) together with an HLLC RHD Riemann solver (Mignone & Bodo 2005). The simulation analysed in this work was run on the Joliot-Curie system at GENCI@CEA, France.

2.1. Simulation Setup

In our model of LS 5039, we simulated the wind dynamics of the system, consisting of a pulsar emitting a relativistic pulsar wind in orbit with a massive O-type star, for three full orbits. Here, we use the same physical parameters for the system as given in Huber et al. (2021b): we adopt the orbital parameters from Casares et al. (2005) using a period of $P_{\text{orbit}} = 3.9$ d, and eccentricity of $e = 0.35$, and masses of $M_{\text{star}} = 23 M_\odot$ and $M_{\text{pulsar}} = 1.4 M_\odot$ (see also Dubus 2013).

As discussed in the introduction, we increased both the extent of the numerical domain and also the spatial resolution in comparison to our previous simulations of LS 5039. With the center of mass at the coordinate origin we use a numerical domain with dimensions $[-2, 2] \times [-0.5, 2.5] \times [-1, 1] \text{ AU}^3$ which is homogeneously filled with $2048 \times 1536 \times 1024$ cubic cells. In total this leads to a resolution of $\sim 0.002 \text{ AU}$ or $\sim 0.42 R_\odot$ in each spatial dimension, i.e. about the same resolution as used in the inner region by Bosch-Ramon et al. (2015) or a doubling of spatial resolution together with a significant increase of the simulation volume in comparison to the previous study by Huber et al. (2021b). In the present study, we use homogeneous resolution throughout the numerical domain. Adaptive mesh refinement was not considered, since small-scale fluctuations filled most of the computational volume (see also Bosch-Ramon et al. 2015).

In our simulation, the z -axis is perpendicular to the orbital plane. As before, the simulation was performed in a reference frame co-rotating with the average angular velocity of the system, which allowed to use a smaller non-symmetric domain than in a non-rotating setup, which contains the full unshocked pulsar wind at all times of the simulation. By using the so-called 3+1 Valencia formulation of general relativistic hydrodynamics (Banyuls et al. 1997), this requires using the source term:

$$\mathbf{S}_m = (\Omega m_y, -\Omega m_x, 0)^\top \quad (7)$$

where Ω is the average angular velocity of the binary (see Huber et al. 2021a, for further details). Since we are dealing with an eccentric orbit in the case of LS 5039, the two stars still show residual motion in the system rotating with the average angular velocity. This is apparent by the axis connecting the binaries not being aligned with the coordinate axes for most of the phases depicted, e.g., in Fig. 1. Periastron is marked by phase $\Phi = 0$,

where the axis connecting the binaries is aligned with the y -axis of our simulation volume.

In the present case, the simulation was performed for 3 full orbits of the system, where the analysis focusses on the second and the third orbit (the first orbit was used to allow the system to change from the initial homogeneous low-density medium to the fully turbulent state). Here, we allowed more time for this initialisation phase than in our previous study because of the larger spatial domain. In the present simulation the undisturbed wind of the massive star reaches the farthest corner of the numerical domain at $t_{\text{crossing}} \approx 0.75 P_{\text{orbit}} \approx 2.9$ d. This is actually a more conservative estimate than in Bosch-Ramon et al. (2015), who initialised most of the domain with the expanding stellar wind, allowing ≈ 0.5 d for initialisation.

For the stellar wind, we used a stellar mass-loss rate of $\dot{M}_s = 2 \cdot 10^{-8} M_{\odot} \text{ yr}^{-1}$ together with a terminal velocity of $v_s = 2000$ km/s (Dubus et al. 2015). The stellar wind was injected as an isotropic outflow in a sphere around the position of the star with radius $r_{\text{inj}} = 0.012$ AU, i.e., with a radius of 6 computational cells, where the star moves in the co-rotating frame due to its eccentric orbit. The pulsar wind was similarly injected with a speed of $v_p = 0.99c$, with c the speed of light. For the pulsar's mass-loss rate we used $\dot{M}_p = \eta \frac{\dot{M}_s v_s}{u_p}$ with $\eta = 0.1$ as also used in Bosch-Ramon et al. (2015). With this, we assume a pulsar spin-down luminosity of $L_{SD} = 7.55 \cdot 10^{28}$ W. The thermal pressure at the outer radius of the injection sphere was set to be a fraction of 10^{-9} and 10^{-7} of the local rest-energy density for the star and the pulsar, respectively.

For analysis we stored 20 output files evenly distributed over orbital phase for each orbit. For a little more than half of these outputs after the first orbit, we produced a series of six successive output datasets with only about 8.3 min between the individual datasets. These can be used to investigate short-term fluctuations and compute statistics of relevant quantities.

3. Results

In Fig. 1 we show the density in the orbital plane for six different phases of the second simulated orbit. In these figures, the dark, mostly featureless region is the radially expanding supersonic pulsar wind, where the bright dot marks the local density peak at the location of the pulsar. The homogeneous region to the left / lower left contains the unshocked, radially expanding stellar wind, where the star is visible as the large bright circle near $(x, y) = (0, 0)$. Between the star and the pulsar, one can see the wind-collision region (WCR), where both winds interact. On both sides, this WCR is bounded by a shock, where the wind-component parallel to the shock normal becomes subsonic. For the stellar wind, this termination shock shows a spiral pattern owing to the orbital motion of the stars. This becomes even more apparent at larger scales as investigated in Bosch-Ramon et al. (2015). The termination shock of the pulsar wind can be split into a u-shaped bow shock and a so-called Coriolis shock formed due to the orbital motion of the system (Bosch-Ramon & Barkov 2011; Bosch-Ramon et al. 2012), where the latter is also a possible site for particle acceleration (Zabalza et al. 2013; Huber et al. 2021b).

In the downstream regions of the WCR, Fig. 1 shows space-filling turbulence, that is driven by different instabilities within the WCR. On the one hand, the shear-flow between the shocked stellar and pulsar winds at the contact discontinuity within the WCR triggers Kelvin-Helmholtz (KH) instabilities (Bosch-Ramon et al. 2012; Lamberts et al. 2013; Bosch-Ramon et al.

2015). Additionally, the Richtmyer-Meshkov (Richtmyer 1960; Meshkov 1972) (RM) and the Rayleigh-Taylor (RT) Rayleigh (1882); Taylor (1950) instabilities are active in this highly dynamical environment, where Bosch-Ramon et al. (2015) discuss that they act together as an important driver of the turbulence in these systems. As is also visible in our Fig. 1 turbulence is much stronger at the leading edge of the WCR (to the left of the cavity containing the unshocked pulsar wind).

This is a strong indication that the RT instability is acting as one of the important drivers of turbulence in these systems, because only at the leading edge do acceleration (by the Coriolis force) and density gradient point in the opposite direction (see also Bosch-Ramon et al. 2015). While Guzdar et al. (1982) point out that a velocity shear will modify the RT instability, they only find a significant reduction of the growth rate for wavelengths shorter than the scale of the density gradient, which in our case is the grid scale. At large scales, where the relevant driving occurs in our simulations, the RT instability is expected to be unaffected by the velocity shear at the contact discontinuity.

The presence of the RT and the RM instabilities is particularly important, since our simulation cannot capture ultra-relativistic Lorentz factors as conventionally expected for pulsar winds (Aharonian et al. 2012; Khangulyan et al. 2012). Since larger Lorentz factors lead to a correspondingly smaller mass-loss rate \dot{M}_p for the pulsar and thus a larger density contrast, we expect longer growth timescales for the KH instability (Ferrari et al. 1980), which is also observed in the classical limit (see, e.g., Chandrasekhar 1961). In contrast, the growth rate of the RT instability depends on the difference of the densities of the stellar and the pulsar wind (see, e.g., Eq. (7) in Allen & Hughes 1984), where the density of the pulsar wind is already negligible in our setup and even more so for larger Lorentz factors. Thus, we expect little change for higher Lorentz factors for the RT instability.

Here, we feature a larger Lorentz factor than Bosch-Ramon et al. (2015), where the turbulence still shows the same general structure in our simulation: we also find ubiquitous turbulence and corresponding mixing downstream of the WCR. Also, in our simulation, we find that the instabilities within the WCR drive the mass loading, i.e. dense matter from the stellar wind is mixed with the dilute, high-velocity pulsar-wind material (see also Bosch-Ramon et al. 2012). This is visible by the dense clumps of shocked stellar-wind material embedded in this region, where in our case the mixing already seems stronger near the apex of the WCR than observed by Bosch-Ramon et al. (2015). Additionally, the fluctuations of the WCR are much stronger than in Bosch-Ramon et al. (2015), where in particular the size of the region containing the unshocked pulsar wind varies more strongly. This difference can be attributed at least to two effects: first, we use a slightly larger eccentricity in our simulation, and secondly, due to the homogeneous resolution in our simulation, turbulence levels in the outer parts of the numerical domain are not damped and can therefore lead to a disruption of the structure of the supersonic pulsar wind volume.

3.1. Coriolis-shock region

The position and structure of the Coriolis shock in our simulation is subject to dynamical changes, as visualised in Fig. 2. There, we show a zoom into the region containing the unshocked pulsar wind over a period of slightly more than 40 min. Apparently, the distance of the Coriolis shock from the apex of the WCR changes significantly, where it is absent for parts of that period, i.e., the flanks of the WCR converge into a point instead of connecting to

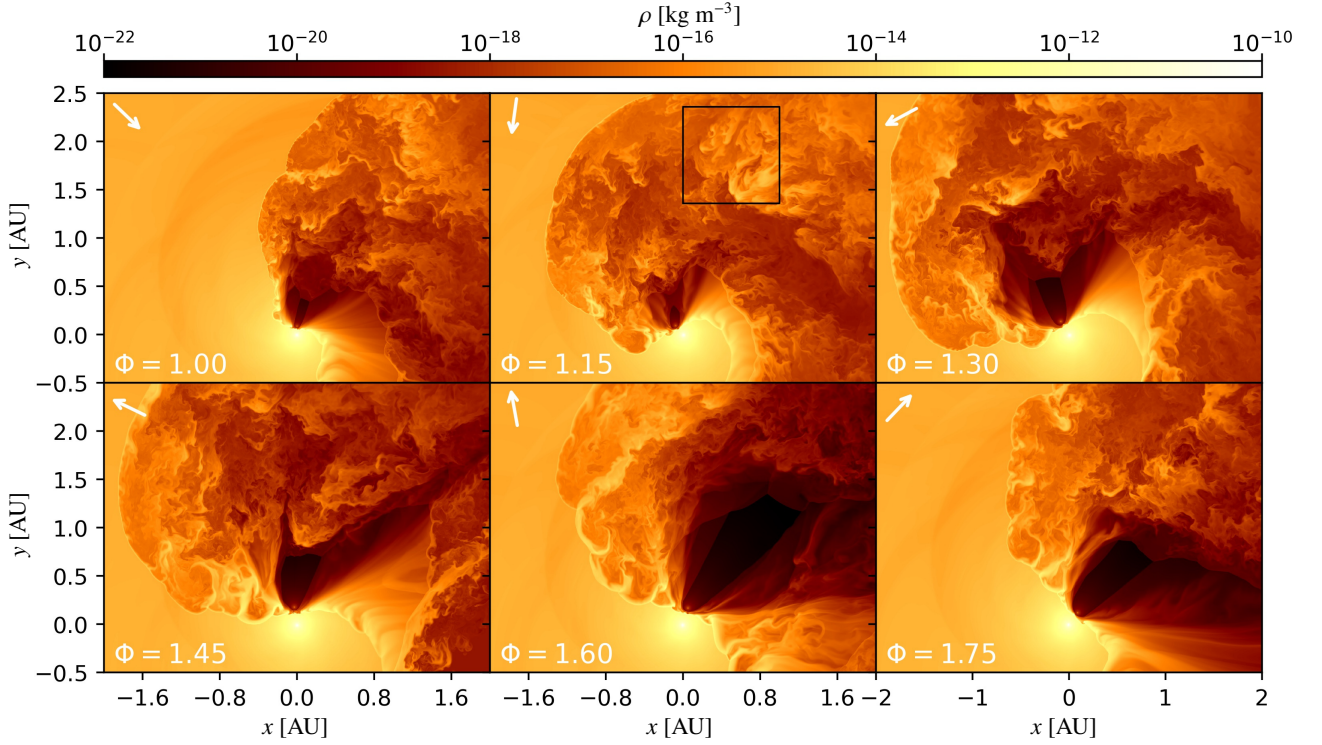


Fig. 1. Mass density in the orbital plane during the second full orbit. Corresponding phases are given in the individual subplots together with an arrow towards the observer location. The center of gravity is at $x = 0, y = 0$. For the central plot at the top, the black box indicates the region, for which we performed the turbulence analysis.

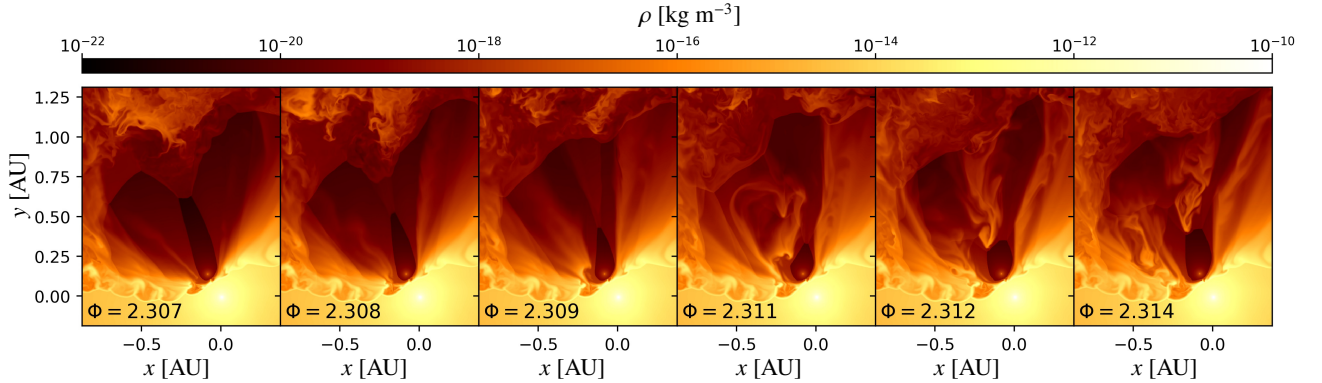


Fig. 2. Different snapshots of mass density in the orbital plane during a short period in the second full orbit as indicated in the plots. As given by the indicated orbital phases, these snapshots cover a period of slightly more than 40 min.

both ends of the Coriolis shock. This will also have implications for particle acceleration at this shock, where a change in distance from the star will also change the energy loss rates of particles at the shock.

Further peculiarities of the shocks in the wind-collision region are visible in Fig. 3, where we show the absolute value of the spatial component of the relativistic four velocity of the fluid $u = \gamma v$. Apparently, sometimes the Coriolis shock marks the transition to a region with the highly turbulent medium containing a mixture of stellar and pulsar wind, while at other phases it is embedded within the relativistic fluid from the wings of the WCR propagating between the unshocked pulsar wind and the contact discontinuity, or in a mixed state (right plot in Fig. 3).

This rather laminar fluid in the wings of the WCR, contains streamlines connecting to the apex of the WCR, where the fluid is re-accelerated by the large pressure gradient (Bogovalov et al.

2008), and streamlines connecting to the flank of the pulsar-wind termination shock, where the velocity component perpendicular to the shock normal is still highly relativistic – in total we find Lorentz factors up to ~ 3 in this region. In all cases, this flow also terminates at an extended shock, when entering the region of highly turbulent, mixed matter downstream of the WCR. The material in this region of mostly laminar flow correspondingly still moves supersonically as can be seen in Fig. 4, where we plot the Mach number in the orbital plane during the second full orbit. The highly turbulent matter beyond the extended shock finally features large fractions of subsonic gas. Also beyond the curved termination shock of the stellar wind, we see large regions of turbulent low-Mach-number flow. Only the trailing-edge region beyond the stellar-wind termination shock features supersonic flow that later terminates in an extended shock. The turbulence

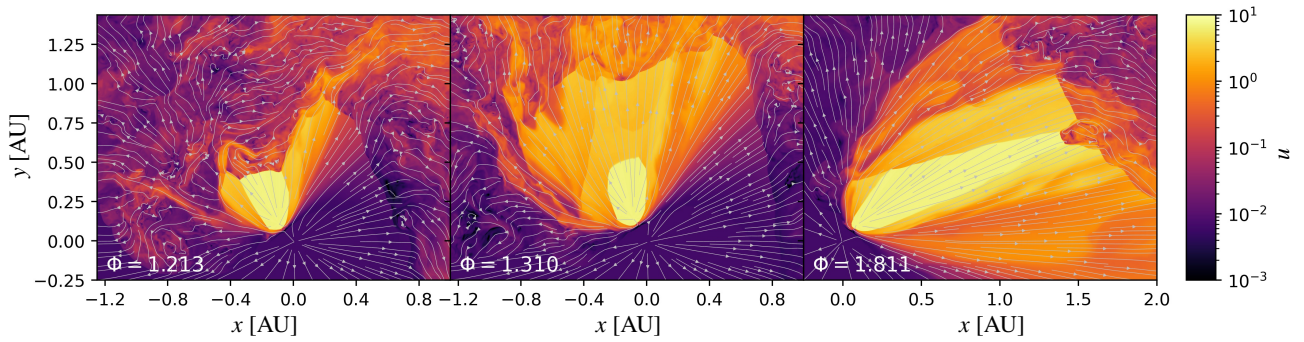


Fig. 3. Absolute value of the spatial component of the fluid's four velocity in the orbital plan at selected phases as indicated in the plots. Superimposed over the images, we indicate the direction of the flow via streamlines. Here, we show a zoom into the computation domain focussing on the region around the Coriolis shock. Be aware of the different x -axis in the right-handed plot.

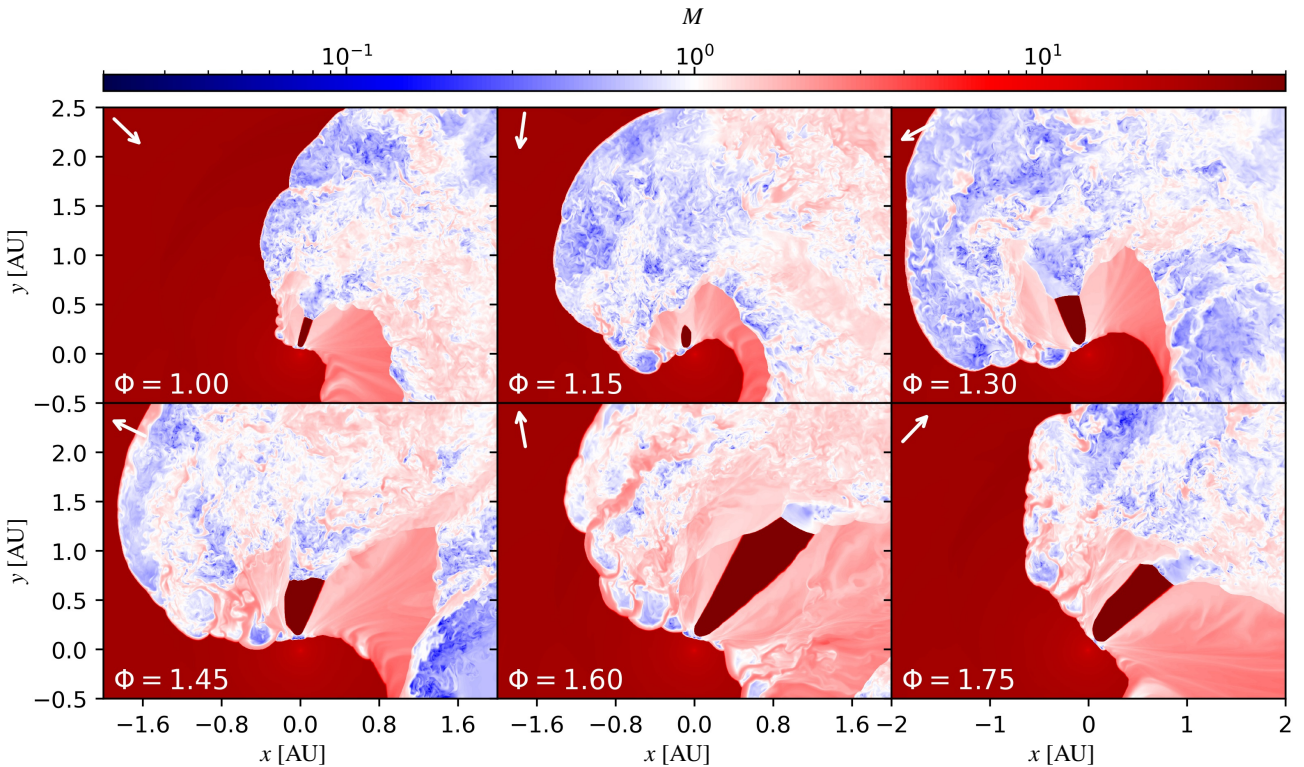


Fig. 4. Mach number in the orbital plane during the second full orbit, for orbital phases as indicated in the subplots. The arrows indicate the direction towards the observer.

beyond these extended shocks is also obvious via the strong fluctuation in the Mach number.

At some times, the region of laminar shocked material is also permeated by large-scale discontinuities, as visible at orbital phases $\Phi = 1.310$ and $\Phi = 1.811$ in Fig. 3. As an example, we show mass density and thermal pressure for $\Phi = 1.310$ in Fig. 5, which feature the same large-scale discontinuity as the flow velocity. Apparently, these discontinuities are shock waves connected to eddies in the contact discontinuity separating the shocked stellar wind from the shocked pulsar wind. By visual inspection it seems that the fluctuations increase beyond the point, where the large-scale shocks traverse the contact discontinuity. Since we do not have outputs at sufficiently short time intervals available to analyse the short-timescale evolution of these fluctuations, this can only be viewed as a hint that the RM instability might be responsible at least for parts of the fluctuations visible in our simulations (see also Bosch-Ramon et al. 2015). Apart

from that, it will be interesting to see how relevant these shock structures are for acceleration and the subsequent non-thermal emission, which has not been studied so far.

3.2. Downstream Flow and Turbulence

Beyond the extended shock structures we observe a highly turbulent downstream region embedded on the left in the unshocked stellar wind. Here, the mixing of stellar- and pulsar-wind material is obvious both in Figs. 1 and 3, where we observe high density clumps from the stellar wind or regions with a high Lorentz factor from the pulsar wind. In our case, this mixing shows up already close to the apex of the WCR, showing the efficiency of the instabilities acting to produce the turbulence. Corresponding statistics is visible in Fig. 6, where we show the distribution function of the Lorentz-factor within the entire numerical domain for different orbital phases.

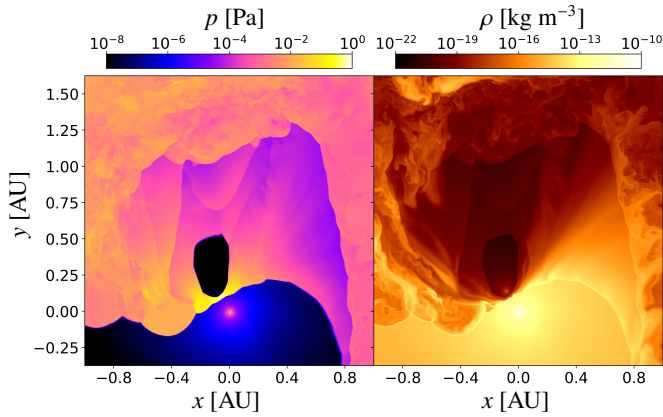


Fig. 5. Pressure (left) and mass density (right) in the region surrounding the unshocked pulsar wind for phase $\Phi = 1.310$.

Given the high resolution together with the homogeneous grid in our simulation, we also investigated the longitudinal structure functions as a measure for the turbulence in our computational domain. Since only the downstream medium shows strong fluctuations, we restricted the corresponding analysis to this region. In particular, we extracted the spatial part of the relativistic four-velocity field from a region with an extent of 1 AU in all spatial dimensions, giving a $512 \times 512 \times 512$ data cube. This subdomain is centred around the orbital plane and located at $x = 0 \dots 1$ AU, $y = 1.36 \dots 2.36$ AU, as indicated via the black box in Fig. 1. The longitudinal structure functions were computed according to (see, e.g. Zrake & MacFadyen 2013)

$$S_p^{\parallel}(l) = \left\langle \left| \frac{1}{l} \delta u^{\mu} \delta x_{\mu} \right|^p \right\rangle \quad (8)$$

where $\delta u^{\mu} = u_2^{\mu} - u_1^{\mu}$ and $l = (\delta x^{\mu} \delta x_{\mu})^{1/2}$ with $\delta x^{\mu} = x_2^{\mu} - x_1^{\mu}$ the separation four vector between pairs of points chosen randomly. Here, we selected points that were simultaneous in the co-rotating frame.

Examples for corresponding structure functions are shown in Fig. 7. We observe only a tiny inertial range, if any, at scales around 0.07 AU, where S_3 in most phases shows a linear dependence on l . Especially for phases just around apastron, the structure functions often show rather erratic behaviour, where we give one of the more well-behaved examples in Fig. 7.

In contrast to homogeneous turbulence simulations, where structure functions are often analysed and show typical behaviour given by the dissipative structures (She & Leveque 1994), the driving in our simulations is not constrained to the largest spatial scales. Instead it follows from the different instabilities, which drive the fluctuations at a range of spatial scales. Therefore, we do not have an extended inertial range in our simulations, where only the effect of the turbulent cascade dominates. Even though most of this driving occurs in the vicinity of the contact discontinuity, the corresponding fluctuations are advected into our analysis regions. This becomes particularly important for orbital phases around and after apastron, where the region filled by unshocked pulsar wind becomes rather large, thus shifting the region with the turbulent driving closer to the turbulence-analysis region. In some of these phases additionally, parts of the unshocked pulsar wind extend into the volume, where we analyse the fluctuations. Despite all this, the structure functions are related to the amplitude of fluctuations within the orbital domain, where we observe strong differences between the different phases depicted in Fig. 7. This strong variability also

observed in the other previous plots, motivates an analysis of the short- and long-term variability of different quantities in this system.

3.3. Short-Term and Orbit-to-Orbit Variations

An important property of our new set of simulation results is the long timescale considered, here. Apart from the initialisation phase in the first orbit, we considered the evolution of the system for two further full orbits. Therefore, we are in a position to quantify dynamical changes during a single orbit as well as orbit-to-orbit variations.

As a first relevant variable that can be easily obtained from the simulation results, we investigated the size of the volume filled with unshocked pulsar wind. This was obtained by adding the volume of all cells with a four velocity fulfilling $\gamma > 7$. As can also be seen in Fig. 3, outside the unshocked pulsar wind such speeds are not achieved despite the re-acceleration of shocked pulsar wind in the flanks of the WCR.

Fig. 8 shows some remarkable features regarding the stability of the unshocked pulsar-wind structure. First, its size apparently is very stable right after periastron. After that, the size expectedly grows, but the fluctuations become very large, especially after apastron. As a measure of the fluctuations we computed the standard deviation of volumes extracted from six consecutive output files. Visual inspection of Fig. 8 shows that this estimate sometimes underestimates the actual variation in our simulations, where strong changes occur at times, for which we have no output data available.

Considering that this is volume and not linear distance, length scales will show correspondingly smaller variations, but it can still be expected that emission from this system will show significantly higher fluctuations around and in particular after apastron. From the given averaged values we find the smallest volume of the unshocked pulsarwind to be 0.0015 AU^3 and the largest, the peak in the third orbit, 0.19 AU^3 . Converting this to a linear distance, this corresponds to a factor of more than 5 in spatial extent, which correlates nicely to the expectation, when considering Fig. 1.

In Fig. 9 we show the orbital variation of the distance of bow and Coriolis shocks from the pulsar. These were computed by following the direction connecting star and pulsar from the pulsar until the Lorentz-factor is smaller than 7. As expected, the distance of the bow shock from the pulsar varies smoothly over the orbit – fluctuations of this distance are small and the variation corresponds to the variation of the orbit. At all phases the distance of the bow shock is at a similar fraction of the approximate distance of the contact discontinuity:

$$d_{CD} = \frac{\sqrt{\eta}}{1 + \sqrt{\eta}} \quad (9)$$

as given by Eichler & Usov (1993). In contrast the distance of the Coriolis shock varies significantly, and not always in accordance with the orbit. Again, strong variations around apastron are present, but also around periastron the variation can be quite large. This again reflects the sudden displacements of the Coriolis shock as shown in Fig. 2 and discussed in Sec. 3. The implications for gamma-ray emission from the particle population related to the Coriolis shock will be investigated in a future study.

The distribution of the Lorentz factor in Fig. 6 also shows distinct orbital variation – related to the variation of turbulence. In this plot, we can also see the variation of the volume of the unshocked pulsar wind, as discussed above, from the changing magnitude of the peak near $\gamma = 7$. The varying fraction

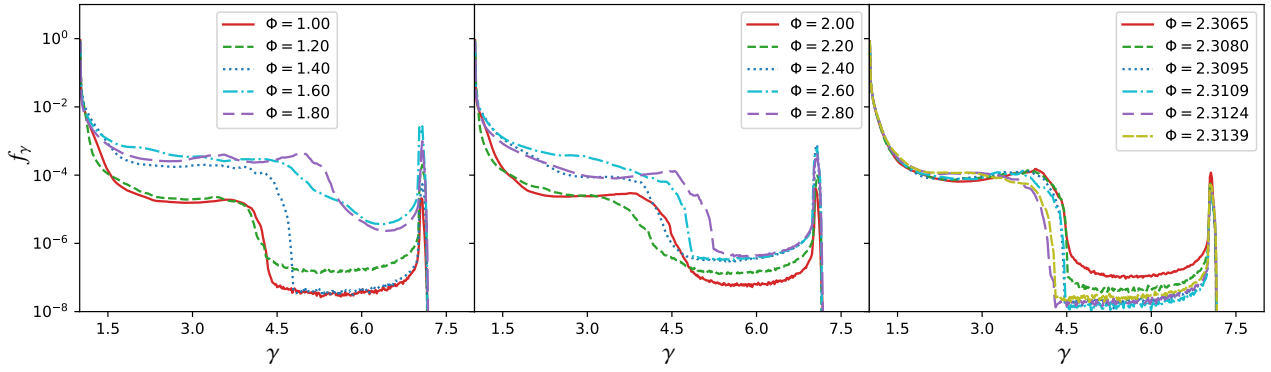


Fig. 6. Distribution function of the relativistic gamma factor f_γ within the orbital domain at different phases as indicated in the plots. Here, we show results for the second orbit (left), for the third orbit (middle), and also for the same short time interval as visualised in Fig. 2 (right).

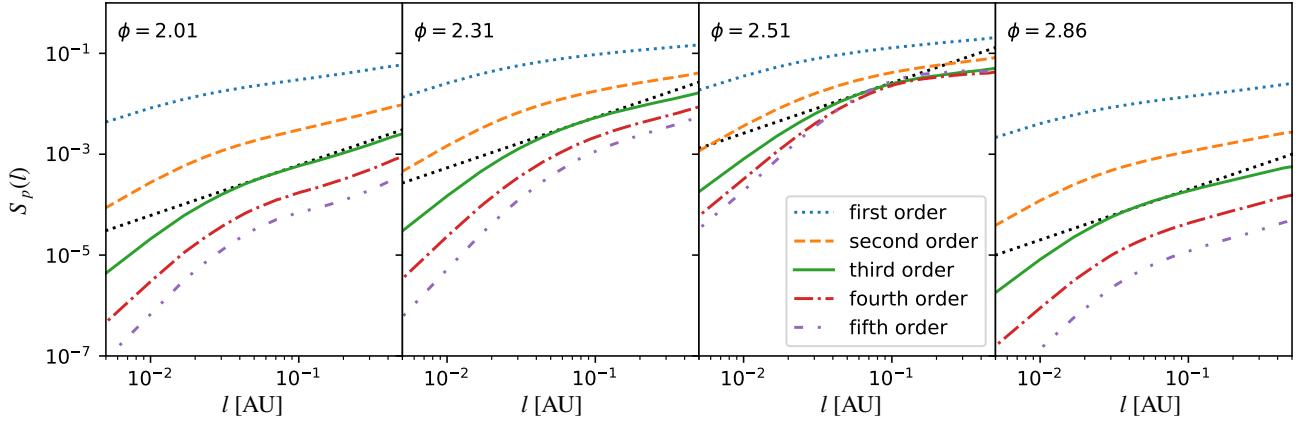


Fig. 7. Structure functions at four different orbital phases as indicated in the figures. For comparison, we show a linear function by the black dotted line. By our normalisation, the structure functions are given in units of c^p .

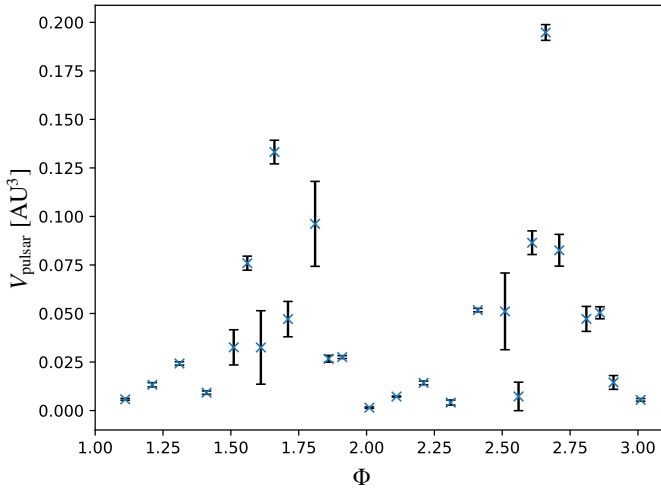


Fig. 8. Volume of unshocked pulsar wind V_{pulsar} as a function of orbital phase Φ . Data are shown for the full second and third orbit. The error bars indicate the corresponding standard deviation, that was computed from multiple output files at similar orbital phases, where we averaged over six phases spread over slightly more than 40 min.

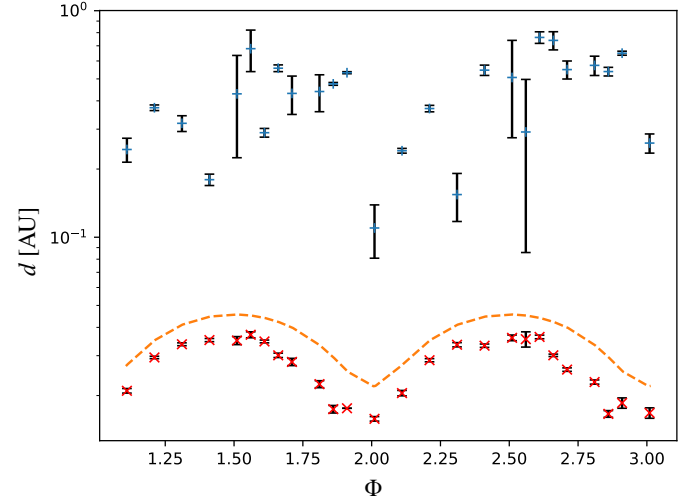


Fig. 9. Distance of the Coriolis shock (blue plus signs) and bow shock (red crosses) from the location of the pulsar as functions of orbital phase, where distances are given along the line connecting star and pulsar. Average values and error bars were determined as stated in Fig. 8. The y-axis uses logarithmic units to allow showing both shock distances simultaneously. Additionally, the dashed orange line shows the approximate distance of the contact discontinuity from the pulsar in the direction of the star using the formula by Eichler & Usov (1993).

of unshocked stellar wind at low gamma factors simply follows through the motion of the stars within the co-rotating domain, which leads to different volumes of unshocked stellar wind as also visible in Fig. 1. The imprint of turbulence can rather be seen at intermediate gamma factors. Also here, the changing volume due to the moving stars has some impact, but apart from

that especially during the second orbit the $4 < \gamma < 7$ regime shows changes related to the dynamics of turbulence, mixing, and dynamical changes of the region around the pulsar-wind ter-

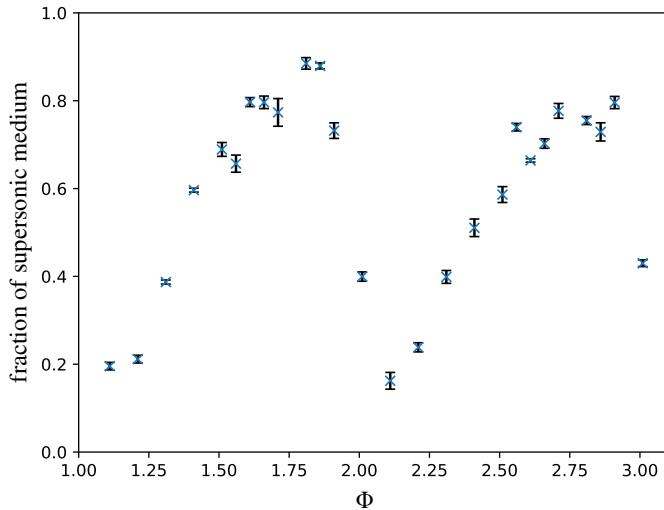


Fig. 10. Fraction of supersonic downstream medium as a function of orbital phase. Average values and error bars were determined as stated in Fig. 8.

mination shock. Apparently, for phases just after apastron, the fraction of shocked pulsar wind in the computational domain is much larger, leading to higher contributions of the intermediate gamma values. Especially at these phases, the unshocked pulsar-wind volume is rather large with a surrounding region of sometimes smooth flow (see Sec. 3.1 and the right-handed figure of Fig. 3), where reacceleration and shocks with large angles between shock normal and pulsar-wind velocity can lead to high gamma factors in this post-shock region.

This behaviour is qualitatively also visible in the third orbit (see middle plot in Fig. 6), but it is less pronounced in this case. This hints at strong orbit-to-orbit variability of the turbulence within this system. Apart from that, we illustrate the short-time variability of the velocity in the right-handed plot of Fig. 6. Apparently, distinct changes of the distribution function of the gamma factor occur even on timescales of a few minutes. In this case, the distribution decreases with time in the region $4 < \gamma < 7$, in accordance with the observations in Fig. 2, where we saw that during this time a large region filled with a smooth high-gamma-factor wind is disrupted and filled with slower, more turbulent matter.

From the distribution of the Mach number in the computational domain, we additionally computed the fraction of supersonic flow in the downstream region. For this, the unshocked stellar was identified by its small speed of sound and the unshocked pulsar wind by its large Lorentz factor. Both unshocked winds were excluded from this analysis since the flow is highly supersonic in each case. As can be seen in Fig. 10, the fraction of downstream medium that moves supersonically in our simulation depends strongly on orbital phase, with a clear peak after apastron. This behaviour is also visible in Fig. 4, where phases near and after apastron feature large regions with high Mach-number flow - especially relating to the smooth flow surrounding the unshocked pulsar wind.

Since neither the mere amplitude of the velocity as given by the distribution of the gamma factor nor the Mach number of the flow do directly give the turbulence amplitude, we additionally computed an estimate for the mean rate of inertial energy dissipation from the third-order longitudinal structure functions S_3 .

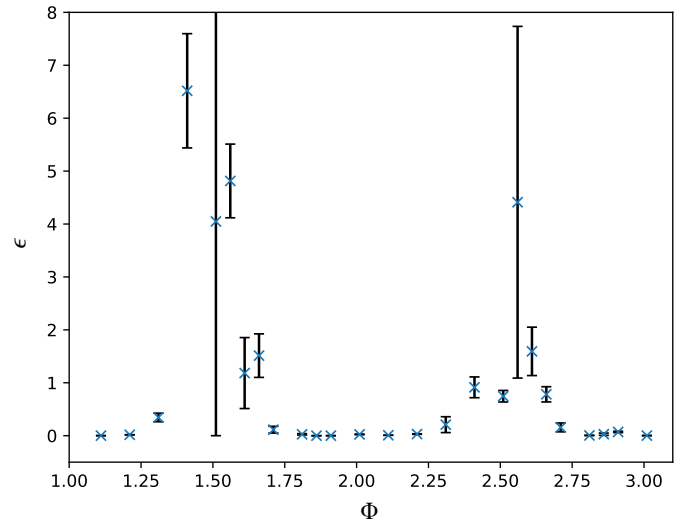


Fig. 11. Variation of the mean rate of inertial energy dissipation per unit mass ϵ as a function of orbital phase Φ over the second and the third orbit. As in Fig. 8, the error bars indicate the standard deviation computed from six consecutive output files. ϵ is given in units of c^3/AU .

Using Kolmogorov's four-fifth law:

$$S_3 = -\frac{4}{5}\epsilon l, \quad (10)$$

ϵ was computed by integrating S_3 over the range of scales, where S_3 follows the expected $S_3 \propto l$ dependence (see Fig. 7), and then solving for ϵ . Its orbital dependence is similar to the previously discussed ones, with peaks around periastron and strong variation around the same time. In particular around apastron, we observed several phases, where the region in which we evaluate the structure functions is permeated by parts of the unshocked pulsar wind. This leads on the one hand to non-turbulent regions within the analysis volume. On the other hand the contact discontinuity is close by the analysis region and is part of it in some cases (more precisely the phases near $\Phi = 1.4 - 1.6, 2.55 - 2.6$ are affected). This also means that the instability driving the turbulence is active within the analysis volume at scales, which are investigated for fully developed turbulence. As a result, the structure functions are not representative for fully developed turbulence. Nonetheless, in nearly all cases, we find $S_3 \propto l$ in the regime from which we compute ϵ . Therefore, we still use the result as a measure of the fluctuations inside the relevant volume. Especially for the phases around apastron we observe strong short-term fluctuations in ϵ .

Apart from the short-time variation discussed so far, we also observe orbit-to-orbit variations. In Figs. 8 - 11, we find that the phase dependence around periastron is very similar in the second and the third orbit. Around apastron, however, the short-term fluctuations are stronger than the orbital ones leading to different phase dependencies in the two investigated orbits. This can also be seen, when comparing the mass density in the orbital plane in the third orbits shown in Fig. 12 to the one in the second orbit shown in Fig. 1. Especially for the shape of the unshocked pulsar-wind region and the immediate surroundings we find strong differences especially after apastron - see the density distributions at $\Phi = 1.6$ vs. $\Phi = 2.6$ or at $\Phi = 1.75$ vs. $\Phi = 2.75$. This corresponds to the times, when we observe large fluctuations in the volume of the unshocked pulsar wind in Fig. 8.

This might also have implications for the variability of non-thermal radiation observed from the system. From our investiga-

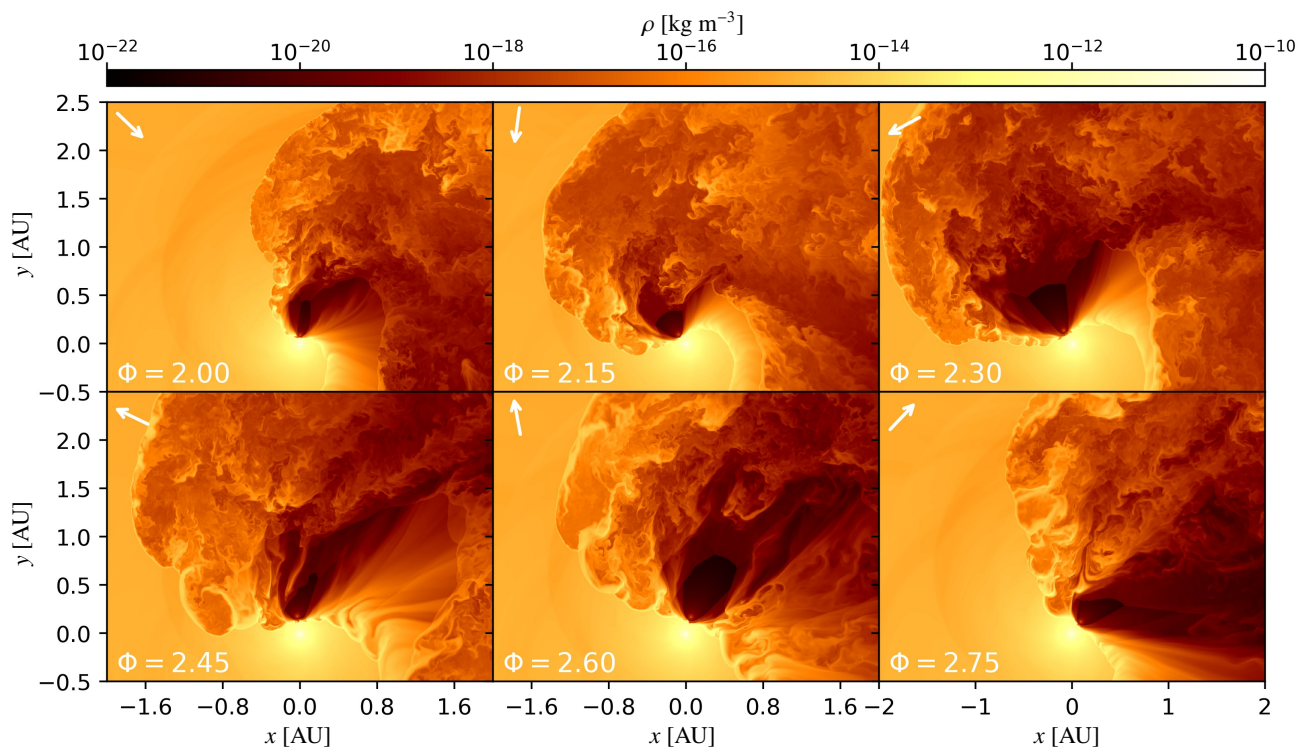


Fig. 12. Same as Fig. 1 but for the third full orbit.

tions of the dynamics of the system, we expect stable gamma-ray emission around periastron with possibly strong variations around apastron. Huber et al. (2021b) found that the gamma-ray emission at the time shortly after apastron is particularly affected by relativistic beaming related to the emission of energetic particles within the leading edge of the shocked pulsar wind. From Figs. 1 and 12, we see that the flow direction in this region is aligned with the direction to the observer some time around relative phase $\Phi = 0.6$, where in the current simulation this situation seems to occur a little later than in the simulations by Huber et al. (2021b). However, as also discussed in Huber et al. (2021b) this phase was not well represented in their simulations due to the limited size of their numerical domain.

This relativistic beaming occurs just in the region, where we have the rather laminar flow within the leading edge of the shocked pulsar wind, which is also visible as the dark yellow region in Fig. 3. That same figure shows that at some phases, there even appear two distinct such regions with different overall flow directions. Regarding the impact on gamma-ray emission, only the relative phases around $\Phi = 0.6$ when the flow is aligned with the observer direction will be important. Due to the rather different structure of this region at phases $\Phi = 1.6$ and $\Phi = 2.6$, however, we can expect to find a different impact of relativistic beaming for the gamma-ray emission in the second and the third orbit. This will be studied in more detail in a forthcoming publication, where we will investigate the propagation of energetic particles within the simulated stellar winds, discussed here. There, it will be particularly interesting if we find short-term and orbit-to-orbit variations on a similar level as we observe in the present study.

4. Summary and Discussion

In this study, we investigated the dynamical interaction of the pulsar wind and the stellar wind in the gamma-ray binary sys-

tem LS 5039 via RHD simulations, where we assumed the wind-driven scenario to explain the observed gamma-ray emission. Here, we did not take the magnetic field in the winds into account, where previous 2D simulations led to the expectation of a rather low impact on the wind dynamics (see the discussion in Bogovalov et al. 2012; Bosch-Ramon et al. 2015). Recent 3D RMHD simulations (Barkov et al. 2022), however, show that for future simulations it will also be interesting to include the effects of the magnetic field. The investigated simulation was done with unprecedented resolution over three full orbits, to allow a detailed analysis of the turbulence driven by the wind-wind interaction in the WCR together with the short-term and long-term variability of the wind dynamics.

In the simulation, we observe strong turbulence in the downstream region of the WCR, where we do not see a clear, broad inertial range due to our driving force by the different instabilities being active at a range of spatial scales. Here, we did not take clumping for the stellar wind into account, which can be shown to further increase fluctuations (Paredes-Fortuny et al. 2015; Kefala & Bosch-Ramon 2023). Thus, short-term and orbit-to-orbit variation might actually be even stronger than found in our model. However, one has to be aware that the Lorentz factor of the pulsar wind, chosen in our and similar simulations, was significantly smaller than expected in a realistic pulsar wind. While this is expected to diminish growth rates for the KH instability (Ferrari et al. 1980), the RM and RT instabilities, which seem to be responsible for a large part of the observed turbulence should be much less affected by a larger Lorentz factor and a corresponding change in density contrast (Allen & Hughes 1984; Bosch-Ramon et al. 2015).

In our configuration we find strong variability due to the turbulence driven within the WCR. While different parameters turn out to be stable around periastron, we observe particularly strong fluctuations both on short and on orbit-to-orbit timescales around apastron. These fluctuations seem to be stronger than found in

previous simulations as, e.g., in Bosch-Ramon et al. (2015). This might be partly attributed to the higher resolution especially in the outer parts of the numerical domain, but also to the somewhat larger eccentricity used in our simulation.

In a future analysis, we will further investigate how the strong dynamics observed here will impact energetic particle transport and ensuing emission of non-thermal radiation from this system. Again the phase shortly after apastron will be particularly interesting, because at this time we observed the largest fluctuations, while it is also the time, where relativistic beaming in the direction of the observer can enhance emission from within the WCR.

Acknowledgements. We thankfully acknowledge PRACE for granting us access to Joliot-Curie at GENCI@CEA, France. We thankfully acknowledge the access to the research infrastructure of the Institute for Astro- and Particle Physics at the University of Innsbruck (Server Quanton AS-220tt-trt8n16-g11 x8). This research made use of Cronos (Kissmann et al. 2018); GNU Scientific Library (GSL) (Galassi et al. 2018); FFTW3 (Frigo & Johnson 2005), matplotlib, a Python library for publication quality graphics (Hunter 2007); Scipy (Virtanen et al. 2020); and NumPy (Harris et al. 2020).

References

- Abdo, A. A., Ackermann, M., Ajello, M., et al. 2009, *ApJ*, 706, L56
- Aharonian, F., Akhperjanian, A. G., Aye, K. M., et al. 2005, *Science*, 309, 746
- Aharonian, F. A., Bogovalov, S. V., & Khangulyan, D. 2012, *Nature*, 482, 507
- Allen, A. J. & Hughes, P. A. 1984, *MNRAS*, 208, 609
- Banyuls, F., Font, J. A., Ibáñez, J. M., Martí, J. M., & Miralles, J. A. 1997, *ApJ*, 476, 221
- Barkov, M. V. & Bosch-Ramon, V. 2016, *MNRAS*, 456, L64
- Barkov, M. V., Kalinin, E., & Lyutikov, M. 2022, *arXiv e-prints*, arXiv:2211.12053
- Bogovalov, S. V., Khangulyan, D., Koldoba, A. V., Ustyugova, G. V., & Aharonian, F. A. 2012, *MNRAS*, 419, 3426
- Bogovalov, S. V., Khangulyan, D. V., Koldoba, A. V., Ustyugova, G. V., & Aharonian, F. A. 2008, *MNRAS*, 387, 63
- Bosch-Ramon, V. & Barkov, M. V. 2011, *A&A*, 535, A20
- Bosch-Ramon, V., Barkov, M. V., Khangulyan, D., & Perucho, M. 2012, *A&A*, 544, A59
- Bosch-Ramon, V., Barkov, M. V., Mignone, A., & Bordas, P. 2017, *MNRAS*, 471, L150
- Bosch-Ramon, V., Barkov, M. V., & Perucho, M. 2015, *A&A*, 577, A89
- Casares, J., Ribó, M., Ribas, I., et al. 2005, *MNRAS*, 364, 899
- Chandrasekhar, S. 1961, *Hydrodynamic and hydromagnetic stability*
- Dubus, G. 2006, *A&A*, 456, 801
- Dubus, G. 2013, *A&A Rev.*, 21, 64
- Dubus, G., Lamberts, A., & Fromang, S. 2015, *A&A*, 581, A27
- Eichler, D. & Usov, V. 1993, *ApJ*, 402, 271
- Ferrari, A., Trussoni, E., & Zaninetti, L. 1980, *MNRAS*, 193, 469
- Frigo, M. & Johnson, S. G. 2005, *Proceedings of the IEEE*, 93, 216
- Galassi, M., Davies, J., Theiler, J., et al. 2018, *GNU Scientific Library Reference Manual*
- Guzdar, P. N., Satyanarayana, P., Huba, J. D., & Ossakow, S. L. 1982, *Geophys. Res. Lett.*, 9, 547
- Harris, C. R., Millman, K. J., van der Walt, S. J., et al. 2020, *Nature*, 585, 357–362
- Harten, A., Lax, P. D., & van Leer, B. 1983, *SIAM Review*, 25, 35
- Huber, D. & Kissmann, R. 2021, *A&A*, 653, A164
- Huber, D., Kissmann, R., Reimer, A., & Reimer, O. 2021a, *A&A*, 646, A91
- Huber, D., Kissmann, R., & Reimer, O. 2021b, *A&A*, 649, A71
- Hunter, J. D. 2007, *Computing in Science & Engineering*, 9, 90
- Kefala, E. & Bosch-Ramon, V. 2023, *A&A*, 669, A21
- Khangulyan, D., Aharonian, F. A., Bogovalov, S. V., & Ribó, M. 2012, *ApJ*, 752, L17
- Kissmann, R., Kleimann, J., Krebl, B., & Wiengarten, T. 2018, *ApJS*, 236, 53
- Lamberts, A., Dubus, G., Lesur, G., & Fromang, S. 2012, *A&A*, 546, A60
- Lamberts, A., Fromang, S., Dubus, G., & Teyssier, R. 2013, *A&A*, 560, A79
- Maraschi, L. & Treves, A. 1981, *MNRAS*, 194, 1P
- Meshkov, E. E. 1972, *Fluid Dynamics*, 4, 101
- Mignone, A. & Bodo, G. 2005, *MNRAS*, 364, 126
- Mignone, A., Bodo, G., Massaglia, S., et al. 2007, *ApJS*, 170, 228
- Paredes-Fortuny, X., Bosch-Ramon, V., Perucho, M., & Ribó, M. 2015, *A&A*, 574, A77
- Rayleigh. 1882, *Proceedings of the London Mathematical Society*, s1-14, 170
- Richtmyer, R. D. 1960, *Communications on Pure and Applied Mathematics*, 13, 297
- Romero, G. E., Okazaki, A. T., Orellana, M., & Owocki, S. P. 2007, *A&A*, 474, 15
- She, Z.-S. & Leveque, E. 1994, *Phys. Rev. Lett.*, 72, 336
- Takahashi, T., Kishishita, T., Uchiyama, Y., et al. 2009, *ApJ*, 697, 592
- Takata, J., Okazaki, A. T., Nagataki, S., et al. 2012, *ApJ*, 750, 70
- Taylor, G. 1950, *Proceedings of the Royal Society of London Series A*, 201, 192
- van Leer, B. 1979, *Journal of Computational Physics*, 32, 101
- Virtanen, P., Gommers, R., Oliphant, T. E., et al. 2020, *Nature Methods*, 17, 261
- Volkov, I., Kargaltsev, O., Younes, G., Hare, J., & Pavlov, G. 2021, *ApJ*, 915, 61
- Yoneda, H., Makishima, K., Enoto, T., et al. 2020, *Phys. Rev. Lett.*, 125, 111103
- Zabalza, V., Bosch-Ramon, V., Aharonian, F., & Khangulyan, D. 2013, *A&A*, 551, A17
- Zrake, J. & MacFadyen, A. I. 2013, *ApJ*, 763, L12

Appendix A: Supplementary material

For further illustration of the dynamics of the system in our simulation, we supply a video of the evolution of the mass density in the orbital plane of the LS-5039 system. The video is produced from the series of six successive outputs for different orbital phases during the full second and third orbit. Since these outputs are not homogeneously distributed over all phases of the orbit, the video continuously jumps from phase to phase, where it shows a brief moment of the short-time dynamics of the system.

This video is useful in showing several of the effects discussed in this paper: the vast difference in speed of the stellar and the pulsar wind becomes directly obvious from the very different short-time motion of the material. Additionally, the highly dynamical changes of the shape and the size of the volume filled by unshocked pulsar wind, becomes very apparent. Finally, only such a video can clearly show the large-scale motion of the material over longer timescales.